A Hybrid Interlayer Reflective Boundary Approximation for Hyperspectral Cloud Radiance Simulation Under Optically Thick Liquid Cloud Conditions

Xiaoyu He , Shilong Jia , Tianjin Liu *

Posted Date: 16 April 2026

doi: 10.20944/preprints202604.1145.v1

Keywords: hyperspectral cloud radiance; radiative transfer; optically thick clouds; extinction-dependent reflective augmentation; forward radiance simulation

 doi:10.20944/preprints202604.1145.v1

Article

A Hybrid Interlayer Reflective Boundary Approximation for Hyperspectral Cloud Radiance Simulation Under Optically Thick Liquid Cloud Conditions

Xiaoyu He, Shilong Jia and Tianjin Liu *

School of Electronic Information Engineering, Beihang University, Beijing, 100191, China

* Correspondence: tianjinliu@buaa.edu.cn;

Highlights

What are the main findings?

- Conventional layered radiative transfer models underestimate hyperspectral cloud radiance under optically thick conditions, particularly in the VIS–SWIR range.
- The proposed extinction-dependent interlayer reflective augmentation significantly improves spectral agreement with GF-5A observations without introducing explicit cloud-boundary assumptions.

What are the implications of the main findings?

- The method provides a fast and physically consistent forward model for hyperspectral cloud radiance simulation, bridging the gap between baseline layered RT and high-cost reference solvers.
- It provides an efficient forward approximation for hyperspectral radiance simulation of optically thick cloud scenes and shows practical potential for hyperspectral image simulation workflows.

Abstract

Accurate simulation of hyperspectral cloud radiance remains challenging under optically thick cloud conditions, where conventional layered radiative transfer (RT) models tend to underestimate cloud-induced backscattering and return radiance in the visible to shortwave infrared (VIS–SWIR) range. In this study, we propose an extinction-dependent interlayer reflective augmentation within a Curtis–Godson (CG)–based layered RT framework. Instead of introducing explicit cloud-top or cloud-bottom boundaries, the method adds a reflective coupling term at all discretized sublayer interfaces, scaled by local extinction properties, to compensate for the underrepresented backward radiative contribution in standard solvers. The proposed approach is designed for optically thick, plane-parallel cloud conditions and aims at improving forward radiance simulation rather than detailed microphysical retrieval. The formulation is constructed so that the reflective augmentation vanishes as the local extinction decreases, although the present experiments focus on optically thick cloud cases. Validation using Gaofen-5A (GF-5A) hyperspectral observations further confirms improved spectral fidelity of simulated cloud radiance in real scenes. Compared with conventional layered RT, the proposed method provides a favorable balance between computational efficiency and accuracy, making it suitable as a fast forward module for hyperspectral cloud radiance simulation of optically thick cloud scenes.

Keywords: hyperspectral cloud radiance; radiative transfer; optically thick clouds; extinction-dependent reflective augmentation; forward radiance simulation

 doi:10.20944/preprints202604.1145.v1

1. Introduction

Unlike active microwave remote sensing systems such as synthetic aperture radar (SAR), which rely on emitted signals to probe surface scattering, passive optical remote sensing measures radiance governed by solar illumination and atmospheric radiative transfer processes [1-3]. Hyperspectral cloud radiance plays a fundamental role in satellite remote sensing, as clouds strongly modulate the top-of-atmosphere (TOA) signal across the visible to shortwave infrared (VIS–SWIR) spectral range and significantly affect the interpretation of surface and atmospheric properties [4–7]. Accurate forward simulation of cloud radiance is therefore essential for applications such as hyperspectral image simulation, atmospheric correction, and cloud-contaminated scene analysis. Under optically thick cloud conditions, TOA radiance is primarily governed by multiple scattering within cloud layers, resulting in strong backscattering and enhanced return radiance toward the sensor [8–11]. Although rigorous radiative transfer (RT) solvers, including discrete ordinates methods, spherical harmonics approaches, and Monte Carlo models, can accurately describe these processes, they are computationally expensive and not well suited for large-scale or real-time hyperspectral simulations [12–14].

A variety of RT approaches have been developed to model cloudy-sky radiance, spanning high-fidelity solvers and fast approximations. In practice, operational forward modeling often relies on simplified plane-parallel layered approximations and parameterized schemes to improve efficiency [15,16]. More recently, fast RT surrogates, neural-network-based forward operators, and simulation-oriented frameworks have been proposed to accelerate hyperspectral radiance modeling while maintaining acceptable accuracy [17–22]. At the same time, recent studies have shown that three-dimensional radiative effects, cloud–environment interactions, and structural cloud heterogeneity can produce non-negligible radiance biases, especially under optically thick conditions [23–27]. These developments indicate that current cloud RT research is increasingly driven by the need to balance physical fidelity and computational efficiency.

Despite these advances, several limitations remain for hyperspectral cloud radiance simulation under optically thick conditions. First, simplified layered approximations may not fully capture the effective backward radiative contribution associated with strong cloud scattering in the VIS–SWIR range [8,9,23]. Second, although three-dimensional RT treatments can better account for cloud-induced radiance perturbations, their computational cost remains prohibitive for large-scale simulation tasks [24–27]. Third, cloud optical thickness, effective radius, and vertical structure all influence radiance formation and retrieval stability, implying that simplified forward assumptions may introduce systematic errors when the actual cloud field departs from idealized conditions [9,12,13]. Fourth, many existing fast approximations are developed for specific retrieval tasks, spectral bands, or simulation settings, and may therefore lack consistent performance across varying cloud optical thickness regimes [15–22]. Therefore, there remains a need for a physically consistent yet computationally efficient forward modeling approach capable of improving hyperspectral cloud radiance simulation under optically thick conditions while remaining compatible with layered radiative transfer solvers used in practical forward modeling.

To address this issue, this study proposes an extinction-dependent interlayer reflective augmentation within a Curtis–Godson (CG)-based layered radiative transfer framework. Rather than introducing explicit cloud-top or cloud-bottom boundaries, the proposed method incorporates an effective reflective coupling term at all discretized sublayer interfaces, parameterized by local extinction properties to account for unresolved backward radiative contributions in conventional layered solvers. The approach is specifically designed for forward radiance simulation in the VIS–SWIR spectral range under optically thick, plane-parallel cloud conditions.

The main contributions of this study are threefold:

1. An extinction-driven reflective augmentation mechanism is developed to enhance cloud-induced backscattering representation without altering the underlying layered radiative transfer structure.

 doi:10.20944/preprints202604.1145.v1

2. The proposed formulation introduces an extinction-dependent reflective augmentation that is fully compatible with the layered radiative transfer solver and improves the representation of cloud-induced backward radiative return under optically thick conditions.
3. The method is systematically validated against both high-fidelity radiative transfer simulations and hyperspectral observations from Gaofen-5A (GF-5A), demonstrating improved spectral fidelity while maintaining computational efficiency.

These characteristics make the proposed approach suitable as a fast forward module for hyperspectral cloud radiance simulation of optically thick cloud scenes in remote sensing applications.

2. Hybrid Reflective Boundary Approximation

The overall computational workflow for hyperspectral cloud radiance simulation is illustrated in Figure 1. The proposed framework takes aerosol, cloud, and atmospheric-state parameters as inputs, together with the viewing geometry and the solar irradiance at the top of the atmosphere (TOA), to construct the forward radiative transfer calculation for cloudy scenes. Specifically, for typical aerosols, the scattering coefficient, absorption coefficient, and scattering phase function are calculated using Mie theory. For atmospheric molecules, the scattering coefficient and phase function are described by Rayleigh scattering theory, whereas the molecular absorption parameters are obtained from spectroscopic databases and the corresponding absorption model. For clouds, the cloud optical properties are derived from cloud microphysical parameters, and an extinction-dependent boundary reflectance term is further constructed to represent the additional reflective contribution associated with strong cloud scattering.

Based on these inputs, the radiative transfer equation is solved within a layered atmosphere framework. In this study, the proposed method is implemented as an extension to the BHU-ATM layered radiative transfer framework, which has been described by the authors' group as an atmospheric radiative transfer model developed in their previous work [28]. Unlike conventional layered radiative transfer treatments, the present method introduces an extinction-dependent reflective augmentation at the interfaces of discretized sublayers under the Curtis–Godson approximation, so as to compensate for the insufficient representation of backward scattering and return radiance under optically thick cloud conditions. The final output of the framework is the upwelling scattered spectral radiance for cloudy scenes.

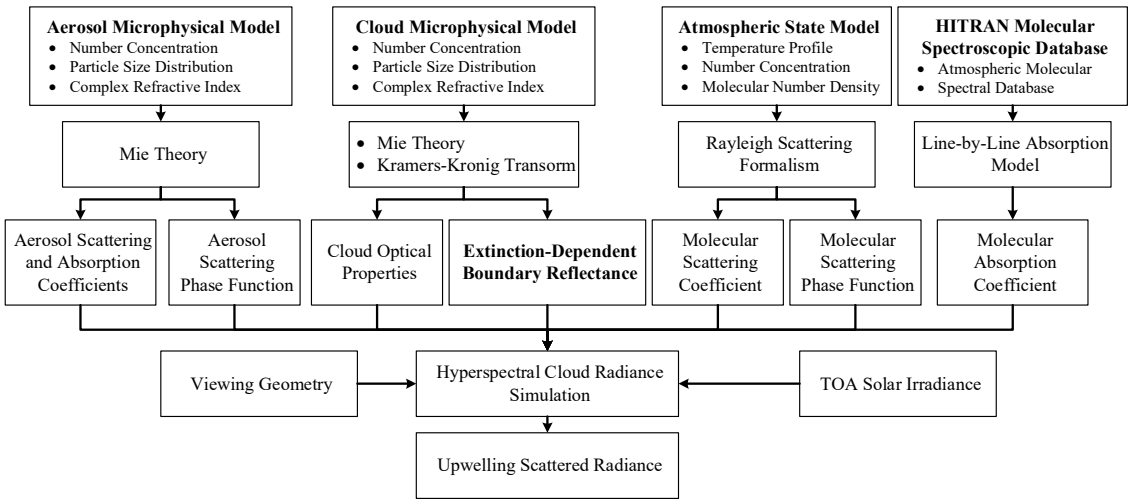

Figure 1. Overall workflow of the proposed extinction-dependent reflective augmentation framework for hyperspectral cloud radiance simulation.

 doi:10.20944/preprints202604.1145.v1

2.1. Baseline Layered Radiative Transfer Formulation

The baseline cloudy-sky radiative transfer calculation adopted in this study is formulated within a vertically layered atmosphere framework. In general, the spectral path radiance is obtained by solving the radiative transfer equation along the observation path, where extinction and source terms jointly determine the radiative transfer process. The source term consists of thermal emission, single scattering, and multiple scattering contributions. Accordingly, the total path radiance can be decomposed into the sum of thermal-emission radiance, single-scattering radiance, and multiple-scattering radiance. For the VIS–SWIR spectral range considered in this study, the thermal contribution is negligible in most bands, and the observed radiance is primarily governed by solar scattering processes.

The path radiance E_p can be described by the radiative transfer equation as

$$\frac{dE_p^{\pm}(\lambda,\nu)}{d\nu} = -E_p^{\pm}(\lambda,\nu) + S(\lambda,\nu) \tag{1}$$

where ν denotes the optical depth; E_p is the path spectral radiance; and S is the source term. The source term can be written as

$$\begin{aligned} S(\theta_v,\phi_v;\theta_s,\phi_s;q) = [1-\omega(q)]\,B[T(q)] + \frac{\omega(q)}{4\pi} P(q,\theta_v,\phi_v;\theta_s,\phi_s)E_0 e^{-q} \\ + \frac{\omega(q)}{4\pi}\int_0^{2\pi}\int_{-1}^{1} P(\theta_v,\phi_v;\theta',\phi';q)E(\theta',\phi';q)\,d\phi'\,d\theta' \end{aligned} \tag{2}$$

where θ_v and ϕ_v are the viewing zenith and azimuth angles; θ_s and ϕ_s are the solar zenith and azimuth angles; q is the optical depth; $T(q)$ is the atmospheric temperature at optical depth q; ω is the single-scattering albedo; P is the scattering phase function; E_0 is the solar spectral irradiance at the top of the atmosphere; and B is the Planck radiance, which can be expressed as

$$B(\lambda,T) = \frac{2\pi hc^2}{\lambda^5}\cdot\left[\exp\left(\frac{hc}{\lambda k_B T}\right)-1\right]^{-1} \tag{3}$$

where h is the Planck constant; c is the speed of light in vacuum; and k_B is the Boltzmann constant.

Based on Equation (2), the path radiance can be decomposed as

$$E_p(\lambda) = E_e(\lambda) + E_s(\lambda) + E_m(\lambda) \tag{4}$$

where E_e, E_s, and E_m denote the thermal-emission, single-scattering, and multiple-scattering components, respectively.

To enable efficient forward modeling, the vertically inhomogeneous atmosphere is approximated by a set of homogeneous sublayers using the Curtis–Godson (CG) approximation. Under this approximation, the thermodynamic and optical properties within each sublayer are assumed to be uniform, and the radiative exchange is solved layer by layer. Let the atmosphere from the surface to the top of the atmosphere be divided into n homogeneous sublayers. Then, the top-of-atmosphere (TOA) upwelling spectral radiance can be expressed as the sum of the attenuated radiative contributions generated in each sublayer along the observation path.

A schematic illustration of the layered radiative transfer process is shown in Figure 2. In the original formulation, the red line denotes the incident solar beam, the black line denotes the radiance received by the sensor, the green lines denote upward scattering, and the blue lines denote downward scattering.

 doi:10.20944/preprints202604.1145.v1

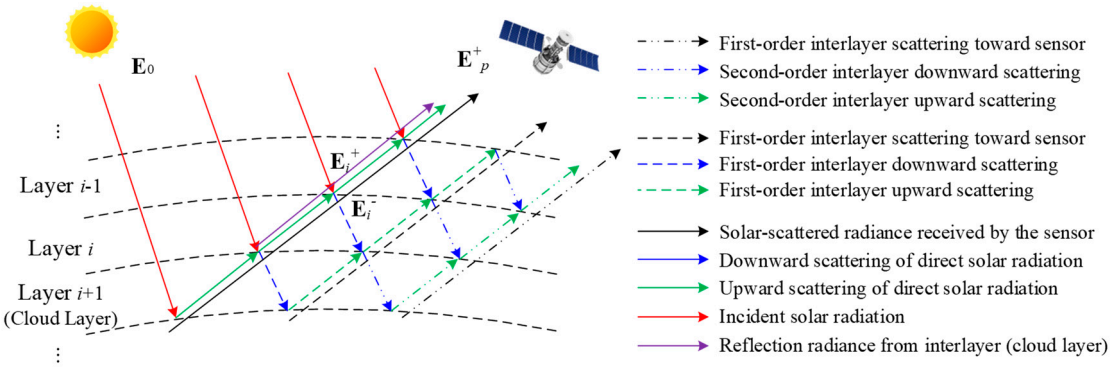

Figure 2. Schematic diagram of the layered radiative transfer calculation.

Under the CG approximation, the TOA upwelling radiance can be written as

$$E_p^+(\theta_v,\theta_s,\phi)=\sum_{i=0}^{m}\exp\left[-\nu_i(\theta_v)\right]\cdot\left[E_{e-i}^+(\theta_v)+E_{s-i}^+(\theta_v,\theta_s,\phi)\right] \tag{5}$$

where E_{e-i}^+ and E_{s-i}^+ denote the upward thermal-emission radiance and upward single-scattering radiance contributed by the i-th sublayer, respectively, and $\nu_i(\theta_v)$ is the optical thickness along the viewing path. The scattering angle ϕ is defined by

$$\cos\phi=\cos\theta_v\cdot\cos\theta_s+\sin\theta_v\cdot\sin\theta_s\cdot\cos(\phi_v-\phi_s) \tag{6}$$

For the i-th homogeneous sublayer, the upward and downward thermal-emission components are assumed to be equal because the temperature and optical properties are constant within the layer under the CG approximation. Therefore, the thermal-emission term can be expressed as

$$E_{e-i}^+(\theta_v)=E_{e-i}^-(\theta_v)=\left[1-\omega_i\right]\cdot B(T_i)\cdot\left[1-\tau_{s-i}(\theta_v)\right] \tag{7}$$

where T_i is the sublayer temperature and τ_{s-i} is the direct transmittance of the i-th sublayer.

In the cloud-free baseline case, the upward and downward single-scattering radiances of the i-th sublayer are written as

$$E_{s-i}^+(\theta_v,\theta_s,\varphi)=E_{d-j}^-(\theta_v,\theta_s,0)\cdot\frac{P_i^+(\varphi)}{4\pi}\cdot\omega_i\cdot\frac{1-\tau_{s-i}(\theta_v)\cdot\tau_{s-i}(\theta_s)}{1+f_i(\theta_s)/f_i(\theta_v)} \tag{8}$$

$$E_{s-i}^-(\theta_v,\theta_s,\varphi)=E_{d-j}^-(\theta_v,\theta_s,0)\cdot\frac{P_i^-(\varphi)}{4\pi}\cdot\omega_i\cdot\frac{1-\tau_{s-i}(\theta_v)\cdot\tau_{s-i}(\theta_s)}{1-f_i(\theta_s)/f_i(\theta_v)} \tag{9}$$

where $j=i-1$ denotes the upper neighboring sublayer; E_{d-j}^- is the total downward radiance transmitted from the $(i-1)$-th sublayer to the i-th sublayer, and P_i^+ and P_i^- represent the upward and downward phase functions of the i-th sublayer, respectively. The total downward radiance entering the next sublayer is then recursively written as

$$E_{d-i}^-(\theta_v,\theta_s,0)=E_{d-j}^-(\theta_v,\theta_s,0)\tau_{s-i}(\theta)+E_{e-i}^-(\theta_s)+E_{s-i}^-(\theta_v,\theta_s,0) \tag{10}$$

with the TOA boundary condition

$$E_{d-0}^-(\theta_v,\theta_s,0)=E_0 \tag{11}$$

This recursive formulation provides an efficient layered solution for cloud-free radiative transfer while preserving the main physical processes associated with solar illumination and atmospheric scattering.

When a cloud-containing sublayer is present, the baseline formulation still follows the same layer-by-layer structure, but the cloud influence is introduced through the optical properties of the corresponding sublayer, including the extinction coefficient, single-scattering albedo, and phase-function-related quantities. In the original cloudy-sky treatment, an additional reflective contribution

 doi:10.20944/preprints202604.1145.v1

is introduced at the cloud-related sublayer interface so that a portion of the incident solar radiance is reflected and added to the upward scattered radiance. The upward and downward single-scattering radiances for a cloud-containing sublayer can therefore be written as

$$E_{s-i}^{+}(\theta_v,\theta_s,\varphi)=E_{d-j}^{-}(\theta_v,\theta_s,0)\cdot\frac{P_i^{+}(\varphi)}{4\pi}\cdot\omega_i\cdot\frac{1-\tau_{s-i}(\theta_v)\cdot\tau_{s-i}(\theta_s)}{1+f_i(\theta_s)/f_i(\theta_v)}+E_{d-j}^{-}(\theta_v,\theta_s,0)\cdot R(\theta_s)\cdot\cos\theta_d \quad (12)$$

$$E_{s-i}^{-}(\theta_v,\theta_s,\varphi)=E_{d-j}^{-}(\theta_v,\theta_s,0)\cdot\frac{P_i^{-}(\varphi)}{4\pi}\cdot\omega_i\cdot\frac{1-\tau_{s-i}(\theta_v)\cdot\tau_{s-i}(\theta_s)}{1-f_i(\theta_s)/f_i(\theta_v)} \quad (13)$$

where $R(\theta_s)$ is the cloud-surface reflectance at solar incidence angle θ_s; and θ_d is the angle between the mirror-reflection direction and the viewing direction. The total downward radiance is correspondingly updated as

$$E_{d-i}^{-}(\theta_v,\theta_s,0)=E_{d-j}(\theta_v,\theta_s,0)\cdot[1-R(\theta_s)]\cdot\tau_{s-i}(\theta_s)+E_{e-i}^{-}+E_{s-i}^{-} \quad (14)$$

Because an explicit solution of the higher-order multiple-scattering term is computationally expensive, the baseline framework adopts an approximate treatment based on layer reflectivity correction. Specifically, the total downward radiance transmitted across adjacent layers is enhanced by a reflectivity-dependent factor to approximately represent cumulative interlayer scattering effects. The recursive expression can be rewritten as

$$E_{d-i}^{-}(\theta_v,\theta_s,0)=\frac{E_{d-j}^{-}(\theta_v,\theta_s,0)\cdot\tau_{s-i}(\theta_s)+E_{e-i}^{-}+E_{s-i}^{-}}{1-\rho_i\cdot\rho_{i+1}} \quad (15)$$

where ρ_i is the reflectivity of the i-th sublayer. Accordingly, the TOA radiance expression can be corrected by incorporating the cumulative reflectivity contribution of all sublayers. Although this treatment improves computational efficiency and partially accounts for multiple-scattering enhancement, the conventional interface formulation may still underestimate the effective backward radiative contribution under optically thick cloud conditions. This limitation motivates the extinction-dependent interlayer reflective augmentation proposed in Section 2.3.

2.2. Cloud Optical Property Parameterization

Cloud optical properties in the present study are parameterized from a set of prescribed cloud microphysical variables rather than retrieved directly from observations. In this work, four representative cloud classes are predefined to describe typical cloudy conditions in hyperspectral radiance simulation. These cloud classes are specified by the cloud-base height z_b, cloud-top height z_t, cloud water content (or particle number concentration) profile, particle size distribution, and complex refractive index. This strategy follows the common practice in atmospheric radiative transfer modeling, where a limited number of representative cloud types are used to construct physically interpretable forward simulations. Standard radiative transfer tools such as MODTRAN and libRadtran similarly describe cloud optical properties through microphysical variables including liquid/ice water content and effective radius [12, 29].

For a cloud layer bounded by z_b and z_t, a normalized vertical coordinate is introduced as

$$\eta=\frac{z-z_b}{z_t-z_b},\qquad z_b\le z\le z_t \quad (16)$$

where $\eta\in[0,1]$. The vertical distribution of cloud water content is described by a prescribed analytic profile function,

$$LWC(z)=LWC_{\max}f(\eta;p_1,p_2) \quad (17)$$

where LWC_{max} denotes the characteristic cloud water content and $f(\eta;p_1,p_2)$ is a shape function controlling the relative vertical structure of the cloud. In the cloud parameterization function used in this study, the two profile parameters α and β determine the location and sharpness of the vertical maximum: p_1 primarily controls the growth of cloud water content above cloud base, whereas p_2

 doi:10.20944/preprints202604.1145.v1

controls the decay toward cloud top. This formulation allows different cloud classes to be represented within a unified framework while preserving interpretable structural differences among shallow, stratiform, and vertically developed clouds. A similar emphasis on vertically resolved liquid cloud profile characterization has also been highlighted in recent cloud-structure studies. [7]

The cloud particle size distribution is described using a modified gamma-type formulation,

$$n(r,z) = A(z)r^{a}\exp\left[-b(z)r\right] \tag{18}$$

where r is the particle radius; $A(z)$ is a scaling factor related to the local particle concentration, and a and $b(z)$ are distribution parameters. In practical implementation, the vertical variation of the size distribution is represented through the effective radius $r_{eff}(z)$, which is prescribed for each cloud class. To account for vertical microphysical inhomogeneity, r_{eff} is allowed to vary with height,

$$r_{eff}(z) = r_b + (r_t - r_b)\,g(\eta) \tag{19}$$

where r_b and r_t are the effective radii near cloud base and cloud top, respectively, and $g(\eta)$ is a monotonic profile function. In this study, this height-dependent effective radius is used to represent the fact that cloud droplets in stratiform and convective clouds may exhibit systematic vertical variation due to condensational growth and entrainment effects. Recent cloud-property retrieval studies likewise emphasize that effective radius and vertical structure are tightly coupled and should not always be treated as vertically uniform. [32]

Given the particle size distribution and refractive index, the bulk cloud optical properties are computed from Mie theory. For each wavelength λ, the extinction coefficient $k_{ext}(\lambda,z)$, scattering coefficient $k_{sca}(\lambda,z)$, and scattering phase function $P(\Theta,\lambda,z)$ are obtained by integrating single-particle Mie quantities over the particle size distribution:

$$k_{est}(\lambda,z) = \int_{r_{\min}}^{r_{\max}} Q_{ext}(\lambda,r,m)\pi r^{2} n(r,z)dr \tag{20}$$

$$k_{sca}(\lambda,z) = \int_{r_{\min}}^{r_{\max}} Q_{sca}(\lambda,r,m)\pi r^{2} n(r,z)dr \tag{21}$$

$$P(\Theta,\lambda,z) = \frac{\int_{r_{\min}}^{r_{\max}} P_{11}(\Theta,\lambda,r,m)Q_{sca}(\lambda,r,m)\pi r^{2} n(r,z)dr}{k_{sca}(\lambda,z)} \tag{22}$$

where Q_{ext} and Q_{sca} are the extinction and scattering efficiencies; m is the complex refractive index; and P_{11} is the Mie scattering phase function term. From these quantities, the single-scattering albedo ω_0 and asymmetry factor g are obtained in the standard manner and are used as direct inputs to the layered radiative transfer solver. This microphysics-to-optics mapping is consistent with operational radiative transfer implementations in which liquid water content and effective radius are translated into bulk optical properties before radiance calculation.

Although four representative cloud classes are implemented in the cloud parameterization function, the present results section focuses on three optically thick liquid cloud types, namely stratus, stratocumulus, and cumulus. Their default geometric and microphysical settings are summarized in Table 1. For each class, the cloud layer is specified by the cloud-base height z_b, cloud-top height z_t, a prescribed vertical water-content (or ice-content) profile, and a height-dependent effective-radius parameterization.

Table 1. Parameter settings of the four representative cloud classes used in the cloud parameterization function.

Cloud type	Phase	z_b (km)	z_t (km)	Vertical profile	Characteristic content (g·m^{-3})	$r_{eff}(z)$ profile	$r_{eff}(z)$ range (μm)
Stratus	Liquid	0.5	1.2	Subadiabatic	q_{top} = 0.25	Power-law	5.0-9.0

 doi:10.20944/preprints202604.1145.v1

Stratocumulus	Liquid	1.0	2.0	Subadiabatic	$q_{top} = 0.35$	Power-law	6.0-11.0
Cumulus	Liquid	1.0	3.0	Beta-type	$q_{peak} = 0.6$	Piecewise	4.5-14.0
Cirrus	Ice	9.0	10.5	Gaussian	$q_{peak} = 0.015$	Linear	15.0-25.0

The purpose of introducing these predefined cloud classes is not to reproduce all possible natural cloud conditions, but rather to provide a compact and physically interpretable set of cloud scenarios for forward hyperspectral radiance simulation. This parameterization also makes it straightforward to extend the model to additional cloud types by modifying the cloud-base/cloud-top heights, the vertical profile parameters, and the effective-radius function. Within the present study, the resulting cloud optical properties serve as the cloud-state input to the baseline layered radiative transfer formulation in Section 2.1 and to the extinction-dependent reflective augmentation introduced in Section 2.3.

2.3. Extinction-Dependent Interlayer Reflective Augmentation

In our previous work [30], the reflective contribution at the atmosphere-cloud interface was modeled by treating the cloud as an equivalent macroscopic object and calculating its spectral Fresnel reflectivity from the complex refractive index. In that framework, the imaginary part of the cloud refractive index was obtained from Mie-derived extinction properties, while the real part was reconstructed using the singly subtractive Kramers-Kronig (SSKK) relation, and the interface reflectance was then determined from the Fresnel equations. The results showed that the cloud-surface reflectivity of representative cloud types was weakly wavelength-dependent in the 0.4–4μm range and was primarily controlled by the incident angle.

Although the whole-cloud reflectivity model provides a useful description of the cloud as a single effective reflective object, it does not explicitly account for the vertically distributed radiative coupling inside a discretized layered atmosphere. In the present study, the reflective contribution is reformulated in a layer-consistent manner. Instead of assigning a single reflectivity to the cloud as a whole, we introduce an additional reflective radiance term at every discretized sublayer interface within the Curtis-Godson layered radiative transfer framework. In this way, the reflective contribution is no longer treated as a bulk property of the entire cloud, but as a local interface contribution linked to the optical state of each sublayer.

Let E_{s-i}^{+} denote the upward single-scattering radiance of the i-th sublayer in the baseline formulation introduced in Section 2.1. In the present method, the augmented upward single-scattering radiance is written as

$$\tilde{E}_{s-i}^{+} = E_{s-i}^{+} + \Delta E_{r,i}^{+} \tag{23}$$

where $\Delta E_{r,i}^{+}$ is the additional reflective radiance introduced at the i-th sublayer interface. Similarly, the total downward radiance transmitted into the next sublayer is modified as

$$\tilde{E}_{d-i}^{-} = E_{d-i}^{-} - \Delta E_{r,i}^{-} \tag{24}$$

where $\Delta E_{r,i}^{-}$ denotes the reflected fraction removed from the transmitted downward radiance. For simplicity, the reflective augmentation is introduced only through the local interface term, while the original baseline expressions for thermal emission and scattering remain unchanged.

The key idea of the present work is to retain the Fresnel-type reflectivity kernel from the previously published whole-cloud model, but to modulate it by a local extinction-dependent weighting factor and apply it to every discretized sublayer interface. Accordingly, the additional reflective radiance is written as

$$\Delta E_{r,i}^{+} = \Gamma_i(\lambda) R_{F,i}(\lambda, \theta_s) \cos\theta_{d,i} E_{d,j}^{-}(\theta_v, \theta_s, 0) \tag{25}$$

where $j=i-1$ denotes the upper neighboring sublayer; $E_{d,j}^{-}$ is the downward incident radiance entering the i-th sublayer; $R_{F,i}$ is the Fresnel reflectivity kernel associated with the i-th interface; and $\theta_{d,i}$ is the

 doi:10.20944/preprints202604.1145.v1

angle between the mirror-reflection direction and the viewing direction. The term $\cos\theta_{d,i}$ is introduced in the same geometric spirit as the conventional reflection treatment in the baseline cloudy-sky formulation, so that the reflective contribution is strongest when the reflected direction is close to the viewing direction. The corresponding reduction of the downward transmitted radiance is written as

$$\Delta E^{-}_{r,i} = \Gamma_i(\lambda) R_{F,i}(\lambda,\theta_s) E^{-}_{d,j}(\theta_v,\theta_s,0) \tag{26}$$

In the above expressions, $R_{F,i}$ is not treated as a constant empirical coefficient. Instead, it inherits the physical meaning of the Fresnel reflectivity term developed in the previous work, where the reflectivity is determined by the cloud refractive index and the incidence angle. In the present study, however, this reflectivity kernel is no longer applied to the cloud as a single object; rather, it is incorporated into each discretized sublayer interface and weighted by the local optical state of that sublayer.

The extinction-dependent weighting factor $\Gamma_i(\lambda)$ is defined as

$$\Gamma_i(\lambda) = 1 - \exp\left[-\alpha\beta_{e,i}(\lambda)\Delta z_i\right] \tag{27}$$

where $\beta_{e,i}(\lambda)$ is the extinction coefficient of the i-th sublayer; Δz_i is the geometric thickness of the sublayer, and α is an empirical scaling parameter controlling the strength of the augmentation. This form ensures that the reflective contribution increases with local extinction and layer thickness, which is physically consistent with the expectation that stronger cloud extinction leads to enhanced backward radiative return.

With equations (25)–(27), the recursive expression for the downward radiance in a cloud-containing sublayer can be rewritten as

$$\tilde{E}^{-}_{d-i}(\theta_v,\theta_s,0) = E^{-}_{d,j}(\theta_v,\theta_s,0)\tau_{s-i}(\theta_s)\left[1-\Gamma_i(\lambda)R_{F,i}(\lambda,\theta_s)\right]\cdot + E^{-}_{e-i} + E^{-}_{s-i} \tag{28}$$

and the upward radiance contribution of the same sublayer becomes

$$\tilde{E}^{+}_{s-i} = E^{-}_{d-j}(\theta_v,\theta_s,0)\cdot\frac{P^{+}_i(\varphi)}{4\pi}\cdot\omega_i\cdot\frac{1-\tau_{s-i}(\theta_v)\cdot\tau_{s-i}(\theta_s)}{1+f_i(\theta_s)/f_i(\theta_v)} + E^{-}_{d-j}(\theta_v,\theta_s,0)\cdot\Gamma_i(\lambda)R_{F,i}(\lambda,\theta_s)\cdot\cos\theta_{d,i} \tag{29}$$

Compared with the previously published whole-cloud reflectivity model, the present formulation has two main differences. First, the reflective contribution is distributed over all discretized sublayer interfaces rather than assigned to a single bulk cloud boundary. Second, the reflective term is weighted by the local extinction of each sublayer, allowing the reflective effect to vary continuously with cloud optical state. As a result, the proposed formulation is naturally compatible with the layered radiative transfer solver and does not require an explicitly prescribed cloud-top reflecting surface.

An important advantage of the present parameterization is that it degenerates smoothly to the baseline formulation as the local extinction vanishes. Specifically

$$\Gamma_i(\lambda) \to 0 \qquad as \qquad \beta_{e,i}(\lambda)\Delta z_i \to 0 \tag{30}$$

which means that the reflective augmentation becomes negligible as the local extinction approaches zero, and the model correspondingly reduces to the conventional layered radiative transfer solution. This property ensures that the proposed augmentation remains fully consistent with the baseline layered formulation outside strongly scattering cloud layers.

2.4. Numerical Implementation

The proposed method is implemented as a layer-by-layer forward radiative transfer procedure for hyperspectral cloud radiance simulation. The numerical workflow consists of four main stages: atmospheric and cloud discretization, optical-property construction, reflective-augmentation calculation, and recursive radiative transfer solution. A schematic overview of the complete workflow is already given in Figure 1.

 doi:10.20944/preprints202604.1145.v1

First, the atmosphere is vertically discretized into homogeneous sublayers using the Curtis–Godson approximation. For each sublayer, the atmospheric molecular absorption coefficient, molecular scattering coefficient, molecular scattering phase function, and aerosol optical properties are calculated or prescribed according to the corresponding atmospheric and aerosol models. Cloud-containing sublayers are identified from the cloud parameterization function described in Section 2.2, which provides the vertical distributions of cloud water/ice content and effective radius. Based on these microphysical quantities, the bulk cloud optical properties of each cloudy sublayer, including the extinction coefficient $\beta_{e,i}(\lambda)$, single-scattering albedo $\omega_i(\lambda)$, and phase-function-related quantities, are computed for every wavelength.

Second, for each discretized sublayer interface, the reflective augmentation term is evaluated according to Equations (25)–(27). In practice, the Fresnel reflectivity kernel $R_{F,i}(\lambda,\theta_s)$ is first computed using the reflectivity model established in the previous work, and is then modulated by the extinction-dependent weighting factor $\Gamma_i(\lambda)$. This produces the effective local reflective contribution associated with the i-th sublayer interface. In cloud-free or weakly scattering layers, $\Gamma_i(\lambda)$ approaches zero and the reflective augmentation becomes negligible. In optically thick cloud layers, the augmentation term increases with local extinction and contributes additional upward radiance to the recursive solution.

Third, the downward and upward radiative quantities are solved recursively across all sublayers. Starting from the top-of-atmosphere boundary condition, the downward radiance is propagated layer by layer according to the baseline formulation in Section 2.1, with the extinction-dependent reflective reduction term introduced through Equation (28). After the downward radiance field is obtained, the upward radiance contribution of each sublayer is evaluated, including thermal emission, single scattering, and the added reflective term defined in Equation (29). The final top-of-atmosphere upwelling spectral radiance is then obtained by summing the attenuated upward contributions of all sublayers along the viewing path.

The numerical implementation is summarized in Algorithm 1.

Algorithm 1. Numerical implementation of the proposed boundary-augmented layered radiative transfer model

Input:

Atmospheric state profiles, aerosol parameters, cloud type and cloud microphysical parameters, wavelength grid, solar-viewing geometry.

Output:

Top-of-atmosphere upwelling spectral radiance $E_p(\lambda)$.

1. Discretize the vertically inhomogeneous atmosphere into homogeneous sublayers using the Curtis–Godson approximation.
2. For each sublayer, compute atmospheric molecular absorption and scattering properties.
3. For each cloud-containing sublayer, generate cloud water/ice content and effective-radius profiles using the cloud parameterization model.
4. Compute bulk cloud optical properties $\beta_{e,i}(\lambda)$, $\omega_i(\lambda)$, and phase-function-related quantities from the cloud microphysical parameters.
5. For each sublayer interface, evaluate the Fresnel reflectivity kernel $R_{F,i}(\lambda,\theta_s)$.
6. Compute the extinction-dependent weighting factor $\Gamma i(\lambda)$ and the corresponding reflective augmentation term.
7. Recursively propagate the downward radiance field from TOA to the lower layers.
8. Recursively compute the upward radiance contribution of each sublayer, including the reflective augmentation term.
9. Sum the attenuated upward contributions of all sublayers to obtain the TOA upwelling spectral radiance.

In the present implementation, the cloud parameterization function and the radiative transfer solver are coupled in a wavelength-by-wavelength manner. For each wavelength, the cloud optical properties and the reflective augmentation term are recalculated using the local cloud state and the

 doi:10.20944/preprints202604.1145.v1

corresponding optical constants. This strategy enables a direct simulation of hyperspectral radiance curves over the VIS–SWIR range while maintaining a consistent physical linkage between cloud microphysics, extinction, and interface reflectivity.

From a computational perspective, the proposed method preserves the basic recursive structure of the original layered solver and therefore introduces only a limited additional cost relative to the baseline model. The main extra computation arises from evaluating the extinction-dependent weighting factor and the interface reflective contribution for each cloudy sublayer. Since these operations are algebraic and performed locally at the interface level, the additional computational burden remains much lower than that of explicitly solving a full three-dimensional or Monte Carlo radiative transfer problem. This property makes the proposed model suitable for large-scale forward simulation and repeated hyperspectral radiance calculations.

Finally, it should be noted that the implementation is designed for forward simulation rather than inversion. The reflective augmentation parameter α in Equation (27) is treated as a model parameter to be specified in the numerical experiments, and its effect on spectral radiance simulation is evaluated in the following sections. Under this implementation, the proposed framework provides a computationally efficient approximation to improve the representation of cloud-induced backward radiative contributions under optically thick conditions, while remaining fully compatible with the baseline layered radiative transfer formulation.

3. Results

3.1. Experimental Configuration and Evaluation Metrics

The model performance was evaluated using three complementary metrics: the root-mean-square error (RMSE), the thresholded mean relative error (TMRE), and Feature Selective Validation (FSV) [31,32]. RMSE was used to quantify the absolute radiance discrepancy over the full spectrum, whereas TMRE was adopted to measure the relative deviation in a numerically stable manner. In addition, FSV was used to assess the agreement between simulated and reference spectra from the perspectives of both overall spectral trend and local spectral features. Compared with conventional mean relative error, the thresholded formulation avoids excessive amplification of the error in strong absorption bands, where the reference spectral radiance may approach zero.

For a spectrum with N wavelength samples, RMSE is defined as

$$RMSE = \sqrt{\frac{1}{N}\sum_{k=1}^{N}\left|E_{sim}(\lambda_k) - E_{ref}(\lambda_k)\right|^2} \tag{31}$$

where $E_{sim}(\lambda_k)$ and $E_{ref}(\lambda_k)$ denote the simulated and reference spectral radiance at wavelength λ_k, respectively.

To stabilize the relative-error evaluation, the threshold parameter is defined as

$$\gamma = 0.01 \max_k \left(E_{ref}(\lambda_k)\right) \tag{32}$$

and the thresholded mean relative error is calculated as

$$TMRE = \frac{1}{N}\sum_{k=1}^{N}\left|\frac{E_{sim}(\lambda_k) - E_{ref}(\lambda_k)}{\max(E_{ref}(\lambda_k), \gamma)}\right| \tag{33}$$

This definition ensures that wavelengths with near-zero reference radiance do not dominate the overall relative-error metric. Finally, FSV was employed as an additional spectral-validation criterion to evaluate whether the proposed method improves not only the absolute radiance level but also the consistency of characteristic spectral structures [33]. In this work, the simulations and spectral comparisons were conducted over the 0.8–2.5 μm range. Although the proposed model is formulated for the VIS–SWIR spectral region, the visible bands were excluded from the present evaluation because the GF-5A observations used for validation are saturated in the visible range.

 doi:10.20944/preprints202604.1145.v1

3.2. Simulated Spectral Radiance of Representative Thick Liquid Cloud Types

To evaluate the proposed method under optically thick cloud conditions, numerical simulations were conducted for three representative thick liquid cloud types, namely stratus, stratocumulus, and cumulus. The comparisons were performed over the 0.8–2.5 μm spectral range, which was selected to match the valid unsaturated GF-5A bands used in this study, since the measured cloud radiance in the visible range is saturated. For all cases, the atmospheric background, aerosol model, and solar-viewing geometry were kept identical. The atmospheric background was specified using the U.S. Standard Atmosphere model, the aerosol contribution was represented by the rural aerosol model, and the solar-viewing geometry was fixed with solar zenith angle, viewing zenith angle, and relative azimuth angle set to θ_s = 27.5°、 θ_v = 0.04°, and $\Delta\phi$ = 18.5°, respectively. Under these conditions, the baseline miniDISORT model, the proposed method, and the full DISORT solution implemented in libRadtran were applied to the same cloud scenes.

Figure 3 presents the simulated top-of-atmosphere spectral radiance for the three representative thick liquid cloud cases. In all three cases, the baseline miniDISORT solution exhibits a pronounced low bias relative to the libRadtran reference over most wavelengths, indicating that the conventional layered treatment systematically underestimates the cloud-induced upwelling radiance under optically thick conditions. By contrast, the proposed method significantly increases the simulated radiance level and reproduces the overall spectral variation of the reference spectrum more faithfully.

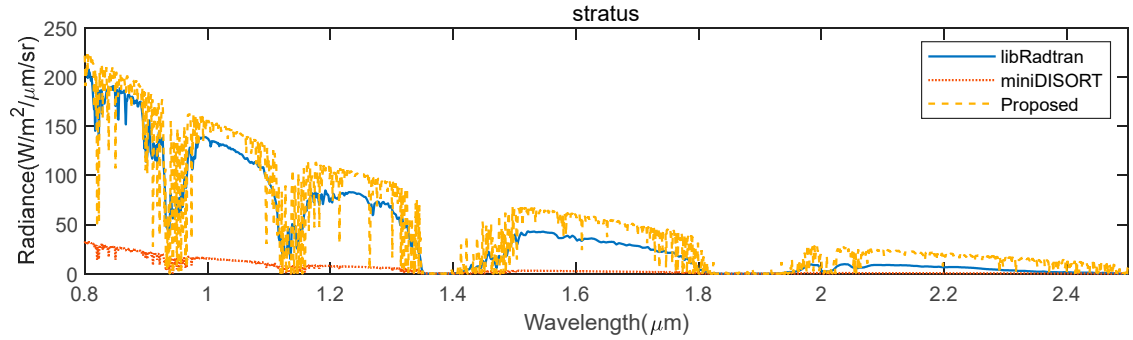

(**a**)

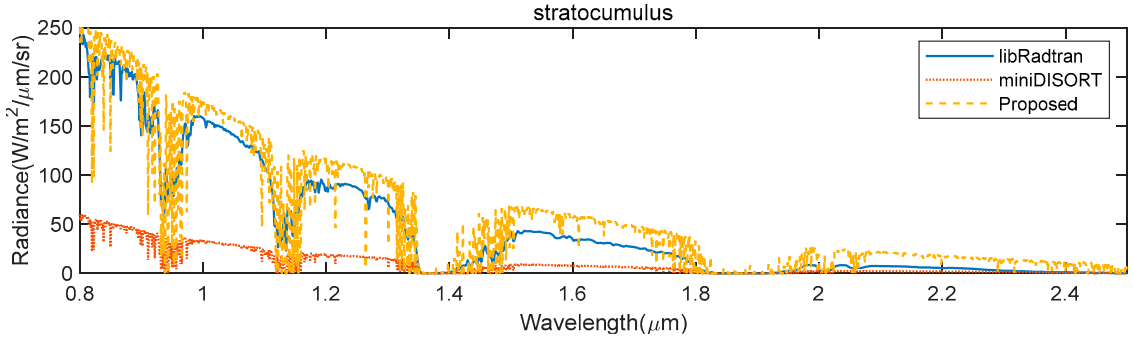

(**b**)

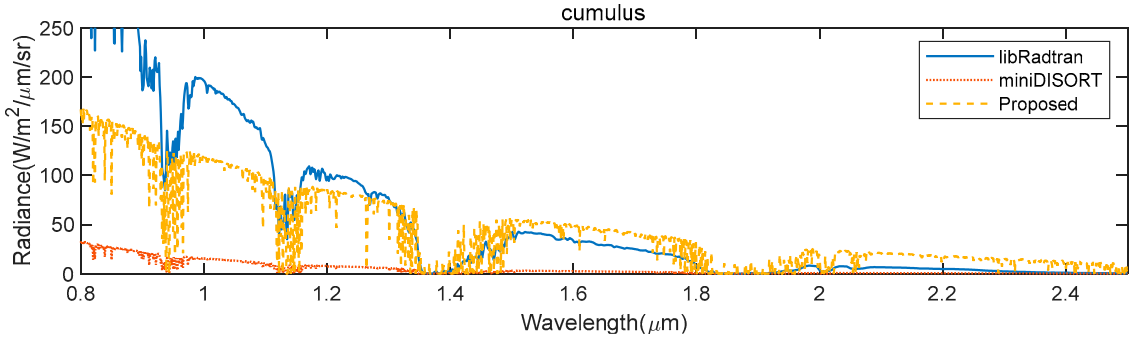

(**c**)

 doi:10.20944/preprints202604.1145.v1

Figure 3. Comparison of simulated TOA spectral radiance for three representative optically thick liquid cloud types in the 0.8–2.5 μm range: (a) stratus, (b) stratocumulus, and (c) cumulus. The libRadtran full DISORT result is used as the reference.

For the stratus case shown in Figure 3(a), the proposed spectrum follows the reference curve more closely across the major transmission windows, while the miniDISORT result remains substantially lower throughout most of the spectrum. The improvement is particularly evident in the 1.0–1.3 μm and 1.5–1.8 μm regions, where the baseline model fails to reproduce the radiance magnitude of the libRadtran solution. Although the proposed curve still shows local overestimation in some wavelength intervals, its overall agreement with the reference is markedly better than that of the baseline model.

A similar behavior is observed in Figure 3(b) for the stratocumulus case. The baseline miniDISORT result again underestimates the radiance over most of the 0.8–2.5 μm range, whereas the proposed method substantially reduces this bias and better captures the spectral structure of the libRadtran reference. The improvement is clear in the major atmospheric transmission windows, although residual discrepancies remain near several absorption-related intervals, where the proposed spectrum exhibits local positive deviations and enhanced fluctuations.

For the cumulus case shown in Figure 3(c), the proposed method also provides a clear improvement over the baseline model, but the agreement with the reference becomes less uniform than in the stratus and stratocumulus cases. In particular, the proposed spectrum remains noticeably lower than the libRadtran result in parts of the 0.8–1.35 μm region, while the agreement improves in the 1.5–1.8 μm and longer-wavelength windows. This result suggests that the reflective augmentation remains effective for vertically developed thick liquid clouds, but the magnitude of the improvement depends on the internal optical structure of the cloud.

A quantitative comparison is summarized in Table 2, where RMSE and TMRE are reported for the three cloud types. For all cases, the proposed method yields lower RMSE and TMRE values than the baseline model, indicating a more accurate reproduction of the absolute radiance level and a more stable relative agreement over the full spectrum.

Table 2. Quantitative Comparison of miniDISORT and proposed approach.

Cloud type	miniDISORT		Proposed	
	RMSE	TMRE	RMSE	TMRE
Stratus	57.7	0.174	21.0	0.078
Stratocumulus	59.7	0.150	21.7	0.068
Cumulus	87.1	0.162	40.9	0.080

Therefore, the proposed method is able to improve the spectral radiance simulation for different classes of optically thick liquid clouds without changing the basic recursive structure of the layered radiative transfer solver.

3.3. Validation with GF-5A Observations

To further assess the practical applicability of the proposed method, validation was conducted using hyperspectral observations acquired by the Advanced Hyperspectral Imager (AHSI) onboard Gaofen-5A (GF-5A). Three cloudy scenes were randomly selected from the available GF-5A dataset. For each scene, cloud regions were first separated using the cloud-detection method reported in the reference [34], and one pixel was then randomly selected from a thick-cloud region for spectral comparison. The original GF-5A files are listed as:

1. GF5A_AHSI_W119.4_N34.3_20240415_007200_L10000116250;
2. GF5A_AHSI_E115.8_N40.7_20251105_015480_L10000353464;
3. GF5A_AHSI_E115.9_N40.2_20251105_015480_L10000353463.

 doi:10.20944/preprints202604.1145.v1

In order to ensure a consistent comparison between the simulated spectra and the GF-5A observations, preprocessing was performed before validation. The simulated spectra were originally generated at a spectral interval of 1 nm, whereas the GF-5A measurements have a spectral resolution of 5 nm in the 0.4–1.0 μm range and 10 nm in the 1.0–2.5 μm range. In the present study, the comparison was restricted to the 0.8–2.5 μm range because the GF-5A measurements in the 0.43–0.8 μm range are affected by radiometric saturation. Accordingly, the simulated spectra were resampled to match the spectral sampling and resolution of the valid GF-5A bands. In addition, because the solar irradiance used in the simulation corresponds to a typical illumination condition rather than the exact illumination level of the observation, the simulated radiance was further corrected using the measured radiance level as a reference, following the same preprocessing strategy described in the GF-5A analysis document. This step was introduced to reduce the influence of illumination mismatch on the subsequent FSV-based comparison.

Figure 4 shows one representative GF-5A cloudy scene, from which multiple cloud pixels were selected for spectral inspection. The extracted pixel spectra clearly indicate that the measured radiance in the 0.43–0.8 μm range is affected by radiometric saturation, which further justifies restricting the subsequent comparison to the 0.8–2.5 μm range.

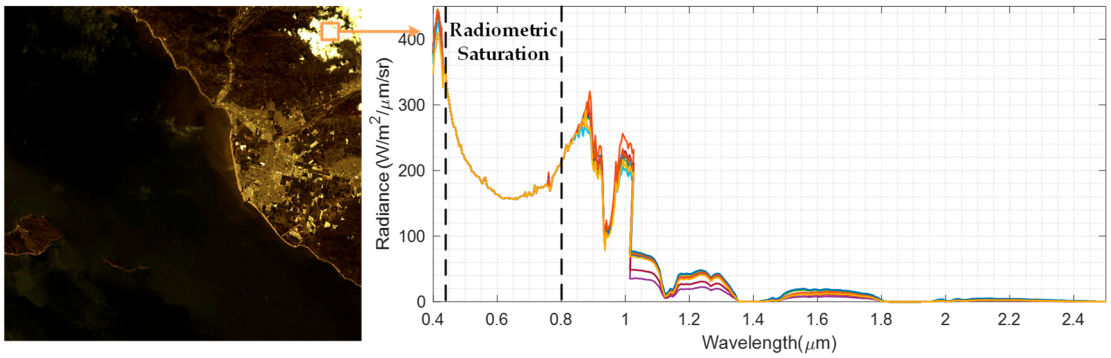

Figure 4. A representative GF-5A cloudy scene and extracted cloud-pixel spectra used for validation, showing radiometric saturation in the 0.43–0.8 μm range.

Figure 5 compares the simulated spectral radiance generated by the proposed method with the measured spectral radiance of the selected cloud pixel. The proposed method reproduces the main spectral trend of the GF-5A observation reasonably well over the valid comparison range. The agreement is stronger in the 1.4–2.5 μm region, whereas the larger residual discrepancies are mainly concentrated in parts of the 0.8–1.4 μm interval.

To quantify the spectral agreement, Feature Selective Validation (FSV) was applied to each scene on a wavelength-by-wavelength basis. Specifically, the Amplitude Difference Measure (ADM), the Feature Difference Measure (FDM), and the Global Difference Measure (GDM) were computed from the simulated and observed spectral radiance curves. Since GDM provides an overall measure that combines both amplitude and feature differences, the GDM curves for the three scenes are presented in Figure 6, while the corresponding ADM and FDM results are summarized statistically in Table 3 and, if needed, provided in the supplementary material. For all three scenes, the GDM values are generally higher near approximately 0.8 μm and 1.2 μm, indicating larger discrepancies in these wavelength intervals, whereas lower values are observed around 1.6 μm, 1.8 μm, and 2.2 μm, where the simulated and measured spectra are more consistent. These results indicate that the proposed method is able to reproduce the major spectral features of thick-cloud radiance, while the remaining mismatches are mainly concentrated in the shorter-wavelength part of the comparison range.

 doi:10.20944/preprints202604.1145.v1

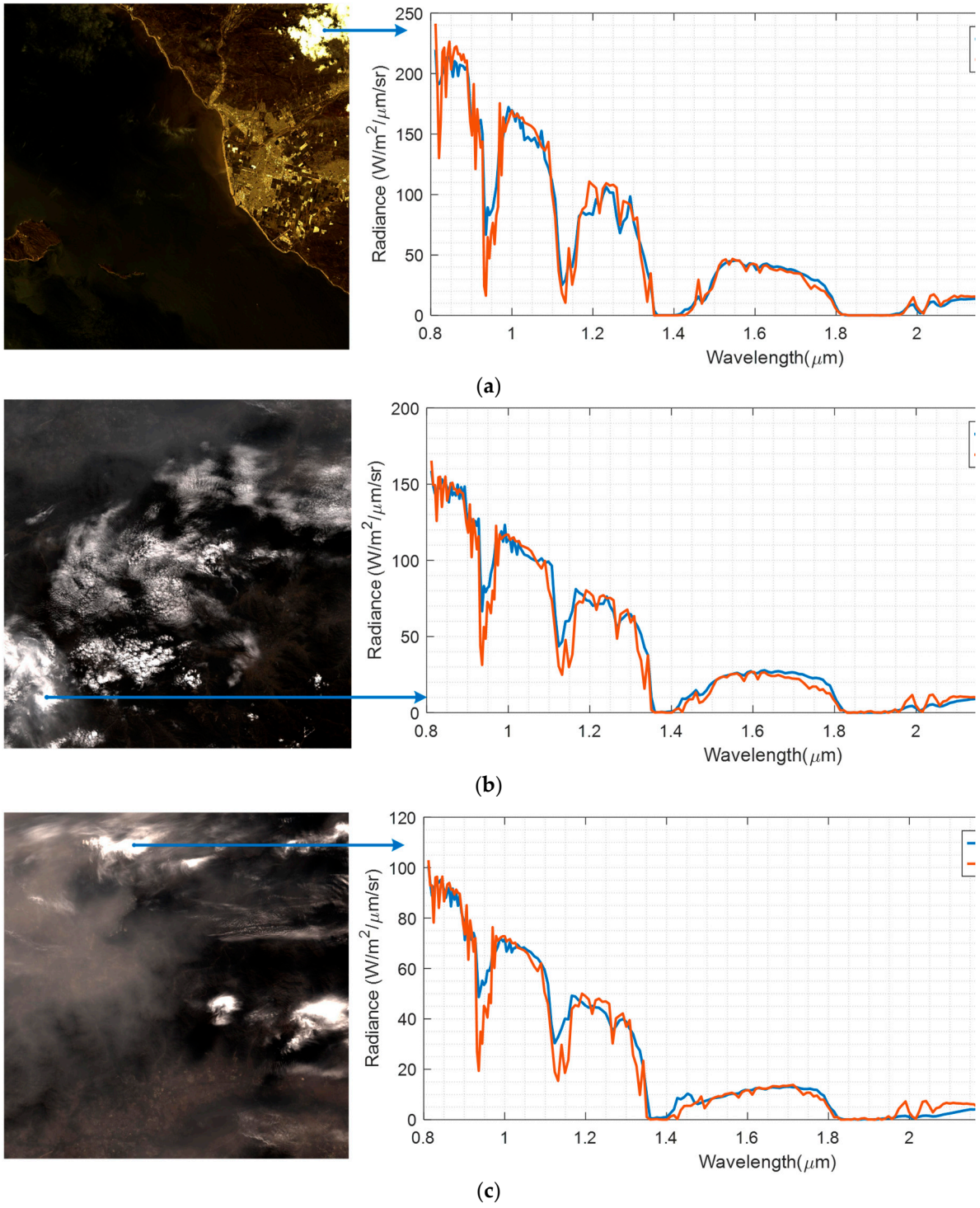

Figure 5. Comparison of the spectral radiance simulated by the proposed method with the measured GF-5A spectral radiance for the selected thick-cloud pixels: (a) Scene 1; (b) Scene 2; (c) Scene 3.

In addition to FSV, RMSE and TMRE were also calculated for the three scenes. Table 3 summarizes the scene-level RMSE, TMRE, mean ADM, mean FDM, and mean GDM values. The RMSE results indicate that the simulated radiance remains at a moderate overall deviation from the GF-5A measurements, whereas the TMRE values provide a stable relative-error estimate even in low-radiance spectral intervals. Together with the FSV statistics, these metrics show that the proposed method can reasonably reproduce the measured thick-cloud hyperspectral radiance of GF-5A and that the agreement is generally stronger in the longer-wavelength part of the comparison range.

 doi:10.20944/preprints202604.1145.v1

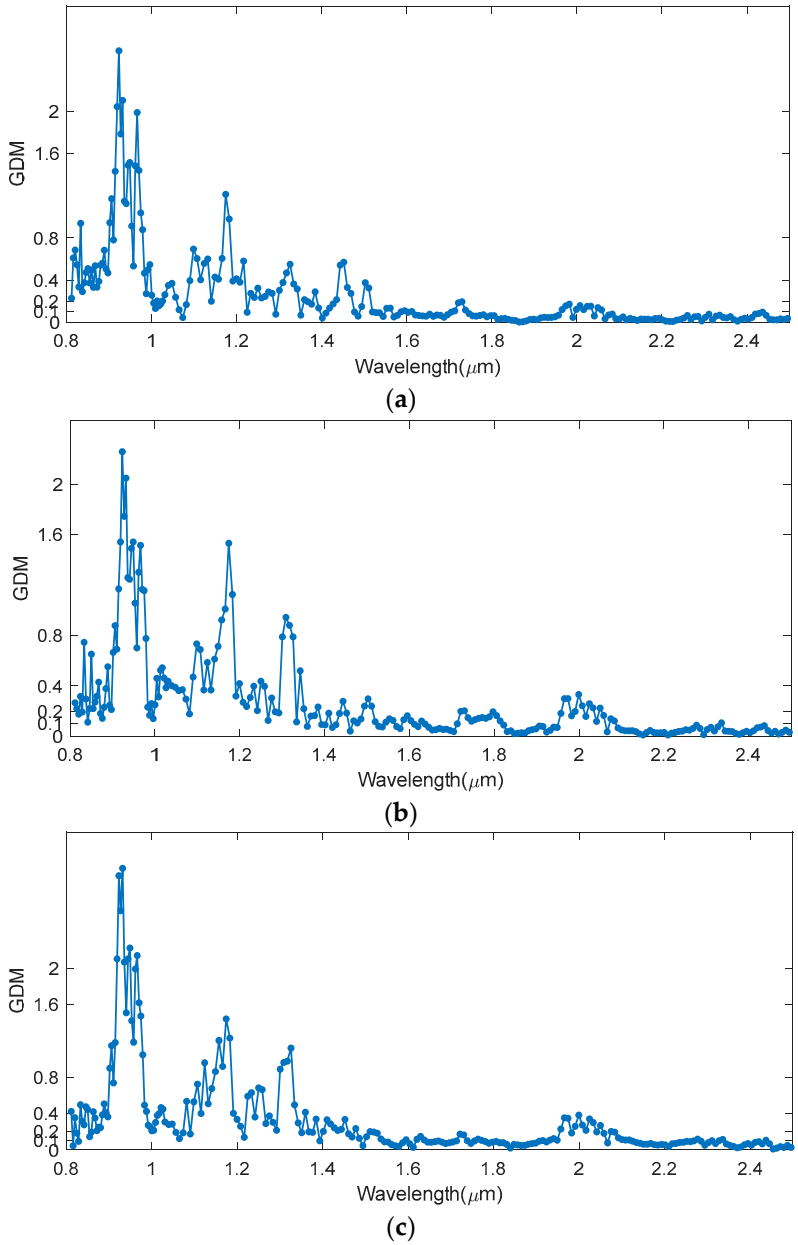

Figure 6. GDM curves of Feature Selective Validation for the three selected GF-5A scenes.

Table 3. Scene-level RMSE, TMRE, and statistical FSV results (mean ADM, mean FDM, and mean GDM) for the three GF-5A scenes.

Scene	RMSE	TMRE	Mean ADM	Mean FDM	Mean GDM
Scene 1	12.2226	0.0313	0.1311	0.3915	0.2920
Scene 2	8.5456	0.0310	0.1549	0.3843	0.2966
Scene 3	5.6834	0.0314	0.1768	0.5112	0.3636

The GF-5A validation demonstrates that the proposed extinction-dependent reflective augmentation provides a physically consistent forward approximation for thick-cloud hyperspectral radiance simulation under practical observation conditions. Although residual discrepancies still exist in several shorter-wavelength intervals, the proposed method is able to capture the main spectral trend and the characteristic spectral features of the measured cloud radiance in all three selected GF-5A scenes.

 doi:10.20944/preprints202604.1145.v1

4. Discussion

4.1. Physical Interpretation of the Spectral Improvement for Representative Thick Liquid Clouds

The results in Figure 3(a–c) indicate that the proposed method consistently reduces the systematic low bias of the baseline layered radiative transfer model for representative optically thick liquid cloud cases. This improvement can be understood from the physical role of the extinction-dependent interlayer reflective augmentation. In the conventional layered formulation, the radiative exchange between adjacent sublayers is mainly controlled by direct transmission, local scattering, and approximate higher-order corrections. Under optically thick cloud conditions, however, strong extinction and repeated backward redirection of radiation tend to enhance the effective return radiance toward the sensor. The baseline model does not fully represent this interface-related reflective contribution, and therefore tends to underestimate the upwelling spectral radiance. By introducing an additional reflective term at each discretized sublayer interface, the proposed method partially restores this missing backward radiative component and raises the simulated radiance toward the high-fidelity reference solution.

The magnitude of the improvement differs among the three cloud cases, which suggests that the effectiveness of the proposed augmentation is closely related to the internal optical structure of the cloud. For the stratus and stratocumulus cases, the cloud layers are relatively compact and vertically smoother, so that the local extinction-driven reflective enhancement acts in a more coherent manner throughout the cloud layer. As a result, the radiance correction is relatively stable across the major transmission windows, and the proposed spectra reproduce both the overall level and the broad spectral variation of the libRadtran reference more closely. In contrast, the cumulus case exhibits stronger vertical inhomogeneity and a more rapidly varying effective-radius profile. Under such conditions, the local reflective augmentation still improves the baseline solution, but the cumulative interface contribution does not match the reference equally well over all wavelengths. This explains why the agreement remains weaker in part of the shortwave near-infrared region, even though a clear improvement is retained in the longer-wavelength windows.

Another feature visible in Figure 3(a–c) is that the improvement is not spectrally uniform. In major atmospheric transmission windows, where the radiance level is relatively high and cloud scattering dominates the signal, the proposed method provides a substantial correction to the baseline low bias. By contrast, in wavelength intervals close to strong absorption features, the enhancement may become less accurate and may even lead to local overestimation or increased fluctuation. Physically, this behavior indicates that the present model captures the extinction-controlled reflective contribution more effectively in scattering-dominated regions than in strongly absorbing regions, where the coupling among molecular absorption, cloud optical thickness, and interface reflection becomes more complicated. Therefore, the remaining residuals do not necessarily imply a failure of the reflective augmentation itself, but rather reflect the simplified nature of the current forward approximation.

Consequently, the three thick-cloud cases demonstrate that the proposed method improves the physical representation of cloud-induced backward radiative return while preserving the computational structure of the baseline layered solver. At the same time, the case-dependent residual discrepancies suggest that the method should be regarded as a physically motivated reduced-order approximation rather than a full substitute for high-fidelity DISORT calculations. Its main value lies in providing a more realistic and computationally efficient forward model for hyperspectral cloud radiance simulation under optically thick liquid cloud conditions.

4.2. Discussion of the GF-5A Validation Results

The GF-5A validation results demonstrate that the proposed method is capable of reproducing the main spectral structure of thick-cloud radiance under real observation conditions, but the degree of agreement is wavelength dependent. A common feature shared by the three scenes is that the simulated spectra match the measured radiance more closely in the 1.4–2.5 μm range than in the 0.8–

 doi:10.20944/preprints202604.1145.v1

1.4 μm range. This behavior is physically reasonable. In the shorter-wavelength near-infrared region, the measured cloud radiance is more sensitive to the detailed cloud-top reflective response, particle-size variability, residual illumination mismatch, and scene-dependent radiometric uncertainty near the saturated visible bands. As a result, even after spectral resampling and radiance correction, the simulated spectra may still exhibit larger deviations from the measurements in this interval. By contrast, in the medium- and long-wavelength part of the comparison range, the spectral response is relatively more stable, and the proposed extinction-dependent reflective augmentation is better able to recover the dominant radiative contribution of optically thick clouds.

The FSV results further support this interpretation. The larger GDM values near approximately 0.8 μm and 1.2 μm indicate that the remaining disagreement is concentrated in a limited number of wavelength intervals rather than being uniformly distributed over the full spectrum. Conversely, the lower GDM values around 1.6 μm, 1.8 μm, and 2.2 μm suggest that the proposed method captures both the amplitude level and the local spectral structure more successfully in these regions. Therefore, the GF-5A comparison does not simply show an overall magnitude match; it also indicates that the proposed method preserves the characteristic shape of the measured cloud spectra in the more reliable part of the observation range.

The scene-to-scene differences observed in the GF-5A validation also suggest that the remaining error is influenced by the actual cloud structure and scene heterogeneity. Since the method represents the cloud field through a one-dimensional layered approximation with extinction-dependent interface reflection, it cannot fully account for horizontal variability, unresolved cloud-edge effects, or more complex three-dimensional radiative interactions within the observed scene. Therefore, the residual mismatch among the three scenes should be interpreted as a combined effect of model simplification, cloud structural complexity, and measurement-side uncertainty, rather than as evidence against the physical validity of the proposed augmentation itself.

These GF-5A results confirm that the proposed method provides a physically meaningful and computationally efficient forward approximation for thick-cloud hyperspectral radiance simulation. Its main advantage lies in improving the representation of cloud-induced backward radiative return under optically thick conditions while remaining compatible with a layered radiative transfer framework. At the same time, the validation results indicate that further improvement is still needed for shorter-wavelength bands and for scenes with stronger spatial heterogeneity.

4.3. Applicability, Limitations, and Future Improvements

The proposed method is mainly applicable to forward hyperspectral radiance simulation of optically thick cloud scenes, especially for liquid clouds that can be reasonably approximated within a one-dimensional layered radiative transfer framework. Under such conditions, the extinction-dependent reflective augmentation provides an effective correction to the systematic low bias of the baseline layered solver while preserving a much lower computational cost than full DISORT calculations.

At the same time, the method should be interpreted as a reduced-order forward approximation rather than a full substitute for high-fidelity radiative transfer modeling. Its present formulation is built on a one-dimensional Curtis-Godson layered representation and therefore does not explicitly account for strong horizontal heterogeneity, unresolved cloud-edge effects, or three-dimensional adjacency effects. In addition, the performance of the method still depends on the prescribed cloud optical properties, including the vertical extinction structure and effective-radius profile, which may contribute to the residual discrepancies observed in both simulated cases and GF-5A validation scenes.

Future improvements may focus on three aspects: refining the extinction-dependent weighting function, incorporating more realistic cloud optical parameterizations, and extending the present framework toward partially three-dimensional correction. These developments may further improve the model performance, particularly in shorter-wavelength bands and in cloud scenes with more complex spatial structure.

 doi:10.20944/preprints202604.1145.v1

5. Conclusions

This study proposed an extinction-dependent interlayer reflective augmentation for hyperspectral cloud radiance simulation under optically thick liquid cloud conditions. Unlike conventional layered radiative transfer formulations, which tend to underestimate the backward radiative contribution of thick clouds, the proposed method introduces an additional reflective term at each discretized sublayer interface within a Curtis-Godson layered framework. In this way, the method enhances the representation of cloud-induced upwelling radiance while preserving the recursive structure and computational efficiency of the baseline solver.

Simulated experiments for representative thick liquid cloud types, including stratus, stratocumulus, and cumulus, showed that the proposed method consistently reduces the systematic low bias of the baseline layered model and improves the agreement with the full DISORT reference. Validation using three GF-5A cloudy scenes further demonstrated that the proposed method is able to reproduce the main spectral trend and characteristic features of measured cloud radiance in the 0.8–2.5 μm range. The agreement is generally better in the 1.4–2.5 μm interval, while larger discrepancies remain in parts of the shorter-wavelength range.

The proposed method provides a physically meaningful and computationally efficient forward approximation for thick-cloud hyperspectral radiance simulation. Although further improvement is still needed for shorter wavelengths and more complex cloud scenes, the present work shows that extinction-dependent interface reflection is a useful mechanism for improving layered cloud radiance modeling and has practical potential for hyperspectral image simulation under cloudy conditions.

Author Contributions: Conceptualization, X.H..; methodology, X.H.; software, S.J.; validation, X.H., S.J. and T.L.; formal analysis, X.H.; investigation, S.J.; resources, X.H.; data curation, X.H.; writing—original draft preparation, X.H. and T.L.; writing—review and editing, X.H. and T.L.; visualization, X.H. and T.L; supervision, X.H.; project administration, X.H.; funding acquisition, X.H. All authors have read and agreed to the published version of the manuscript.

Funding: This research was funded by the National Natural Science Foundation of China under grant number 62001017.

Conflicts of Interest: The authors declare no conflicts of interest.

References

1. Liou, K. N. *An Introduction to Atmospheric Radiation*, 2nd ed.; Academic Press: San Diego, CA, USA, 2002.
2. Liou, K.N. Radiation and Cloud Processes in the Atmosphere: Theory, Observation, and Modeling; Oxford University Press: New York, NY, USA, 1992.
3. Bucholtz, A. Rayleigh-scattering calculations for the terrestrial atmosphere. *Appl. Opt.* **1995**, 34(15), 2765–2773.
4. Liu, Y.; Sun, D.; Cao, K.; Liu, S.; Chai, M.; Liang, J.; Yuan, J. Development of Visible and Short-Wave Infrared Advanced Hyperspectral Imager Onboard GF-5 Satellite. *J. Remot. Sens.* **2020**, *24*(4), 333-344.
5. Liu, Y.; Sun, D.; Cao, K.; Liu, S.; Chai, M.; Liang, J.; Yuan, J. Evaluation of GF-5 AHSI on-orbit instrument radiometric performance. *J. Remote Sens.* **2020**, 24(4), 352–359.
6. Ye, B.; Tian, S.; Ge, J.; Sun, Y. Application of lithological mapping based on advanced hyperspectral imager data from the Gaofen-5 satellite. *Remote Sens.* **2020**, 12(23), 3990: 1-19.
7. Hünerbein, A.; Bley, S.; Deneke, H.; Meirink, J. F.; van Zadelhoff, G.-J.; Walther, A. Cloud optical and physical properties retrieval from EarthCARE multi-spectral imager: The M-COP products. *Atmos. Meas. Tech.* **2024**, 17, 261–276.
8. Quaglia, F.C.; Muscari, G.; Meloni, D.; Bernardino, A. D.; Iorio, T D..; Pace, G.; Schmidt, K.S.; Sarra, A di. On the retrieval of cloud optical thickness from spectral radiances: A sensitivity study with high-albedo surfaces. *J. Quant. Spectrosc. Radiat. Transf.* **2024**, 326, 109108: 1-11.

 doi:10.20944/preprints202604.1145.v1

9. Hu, L.; Yao, B.; Teng, S.; Sohn, B.-J.; Jin, H.; Liu, C. Visible and shortwave-infrared spectral characteristics of mixed-phase clouds in typical satellite radiometer channels. *Atmos. Ocean. Sci. Lett.* **2025**, 18(4), 100588: 1-6.
10. Meyer, K.; Platnick, S.; Arnold, G.T.; Amarasinghe, N.; Miller, D.; Small-Griswold, J.; Witte, M.; Cairns, B.; Gupta, S.; McFarquhar, G.; O'Brien, J. Evaluating spectral cloud effective radius retrievals from the enhanced MODIS airborne simulator during ORACLES. *Atmos. Meas. Tech.* **2025**, 18, 981–1011.
11. Buggee, A.J.; Pilewskie, P. Retrieving vertical profiles of cloud droplet effective radius using multispectral measurements: Examples and limitations. *Atmos. Meas. Tech.* **2025**, 18, 5299–5320.
12. Mayer, B.; Kylling, A. Technical note: The libRadtran software package for radiative transfer calculations–description and examples of use. *Atmos. Chem. Phys.* **2005**, *5*, 1855-1877.
13. Stamnes K.; Tsay S.; Wiscombe W.; Jayaweera, K. Numerically stable algorithm for discrete-ordinate-method radiative transfer in multiple scattering and emitting layered media. *Appl Opt.* **1988**, ;27(12), 2502-2509.
14. Evans, K. F. The Spherical Harmonics Discrete Ordinate Method for Three-Dimensional Atmospheric Radiative Transfer. *J. Atmos. Sci.*, **1998**, 55, 429–446.
15. Chen, Y.-W.; Schmidt, K.S.; Chen, H.; Massie, S.T.; Kulawik, S.S.; Iwabuchi, H. Mitigation of satellite OCO-2 CO_2 biases in the vicinity of clouds with 3D calculations using the Education and Research 3D Radiative Transfer Toolbox (EaR3T). *Atmos. Meas. Tech.* **2025**, 18, 1859–1884.
16. Ademakinwa, A.S.; Tushar, Z.H.; Zheng, J.; Wang, C.; Purushotham, S.; Wang, J.; Meyer, K.G.; Várnai, T.; Zhang, Z. Influence of cloud retrieval errors due to three-dimensional radiative effects on calculations of broadband shortwave cloud radiative effect. *Atmos. Chem. Phys.* **2024**, 24, 3093–3114.
17. Tijhuis, M.; van Stratum, B.J.H.; van Heerwaarden, C.C. The impact of coupled 3D shortwave radiative transfer on cloud development and surface radiation. *Atmos. Chem. Phys.* **2024**, 24, 10567–10582.
18. Várnai, T.; Marshak, A. Observations of three-dimensional radiative effects that influence MODIS cloud optical thickness retrievals. *J. Atmos. Sci.* **2002**, 59(9), 1607–1618.
19. Zhou, Y.; Cao, T.; Zhu, L. Optimizing cloud optical parameterizations in radiative transfer for TOVS (RTTOV v12.3) for data assimilation of satellite visible reflectance data: An assessment using observed and synthetic images. *Atmos. Meas. Tech.* **2025**, 18, 3267–3285.
20. Atarita, F.; Braun, A. An open-source toolkit for hyperspectral remote sensing forward modelling. *Remote Sens.* **2026**, 18(6), 943: 1-21.
21. Butali, E.; Del Bianco, S.; Cortesi, U.; Di Natale, G.; Ridolfi, M. Extending the KLIMA radiative transfer model to cloudy atmospheres: Towards an all-sky analysis of FORUM. *Remote Sens.* **2026**, 18(6), 960: 1–17.
22. Barker, H.W.; Cole, J.N.S.; Villefranque, N.; Qu, Z.; Velázquez Blázquez, A.; Domenech, C.; Mason, S.L.; Hogan, R.J. Radiative closure assessment of retrieved cloud and aerosol properties for the EarthCARE mission: The ACMB-DF product. *Atmos. Meas. Tech.* **2025**, 18, 3095–3107.
23. Herrero-Anta, S.; Román, R.; González-Fernández, D.; Emde, C.; Mateos, D.; Herrero del Barrio, C.; González, R.; Dubovik, O.; Toledano, C.; Calle, A.; Cachorro, V.E.; de Frutos, Á.M. Impact of cloud presence on sky radiances and the retrieval of aerosol properties. *Atmos. Res.* **2025**, *317*, 107938: 1-177.
24. Weber, A.; Köcher, G.; Mayer, B. Parameterization of 3D cloud geometry and a neural-network-based fast forward operator for polarized radiative transfer. *Atmos. Meas. Tech.* **2025**, 18, 5805–5821.
25. Verrelst, J.; Morata, M.; García-Soria, J.L.; Sun, Y.; Qi, J.; Rivera-Caicedo, J.P. RTM surrogate modeling in optical remote sensing: A review of emulation for vegetation and atmosphere applications. *Remote Sens.* **2025**, 17(21), 3618: 1-29.
26. Huang, H.; Wang, Q.; Liu, C.; Zhou, C. Optimal estimation of cloud properties from thermal infrared observations with a combination of deep learning and radiative transfer simulation. *Atmos. Meas. Tech.* **2024**, 17, 7129–7141.
27. Wang, G.; Ye, S.; Xu, B.; Zhi, X.; Liu, Q.; Liu, Y.; Pan, Y.; Fan, C.; Zhang, T.; Xie, F. Generalized variational retrieval of full field-of-view cloud fraction and precipitable water vapor from FY-4A/GIIRS observations. *Remote Sens.* **2025**, 17(22), 3687: 1-27.
28. He, X. Research on Modeling Methods for Earth-Background Hyperspectral Imaging Characteristics. Ph.D.Thesis; Beihang University, Beijing, China, 2018.

 doi:10.20944/preprints202604.1145.v1

29. Berk, A.; Anderson, G.P.; Acharya, P.K.; et al. MODTRAN4 Version 3 Revision 1 User's Manual; Air Force Research Laboratory: Hanscom AFB, MA, USA, 2003. Available online: https://home.cis.rit.edu/~cnspci/references/berk2003.pdf.
30. Jia, S.; He, X. Modeling of spectral Fresnel reflectivity of water and ice cloud using the Kramers-Kronig relation. *Proc. SPIE*, **2025**, 13668, 136680T: 1-11.
31. Duffy, A.P.; Martin, A.J.M.; Orlandi, A.; Antonini, G.; Benson, T.M.; Woolfson, M.S. Feature Selective Validation (FSV) for validation of computational electromagnetics (CEM). Part I—The FSV method. *IEEE Trans. Electromagn. Compat.* **2006**, 48(3), 449–459.
32. Orlandi, A.; Duffy, A.P.; Archambeault, B.; Antonini, G.; Coleby, D.E.; Connor, S. Feature Selective Validation (FSV) for validation of computational electromagnetics (CEM). Part II—Assessment of FSV performance. *IEEE Trans. Electromagn. Compat.* **2006**, 48(3), 460–467.
33. Shuai, S.; Ma, J.; Liu, J.; He, X.; Xu, X. Multiresolution components fused evaluation for hyperspectral atmospheric radiative transfer model using feature selective validation. *Proc. SPIE*, **2024**, 1319, 131990C: 1-11.
34. Song, W; Jia, S.; Liu T.; and He X. Hierarchy Clustering for Cloud Detection Assisted by Spectral Features of Ground Covers. *Remote Sens.* **2026**, 18, 698: 1-20.
35. Gao F.; Ma W.; Yuan C.; Wang J.; Sun J.; Hussain A. Universal domain adaptation for simulation-assisted SAR target recognition based on adversarial uncertainty and neighbor relation. *IEEE Trans. Aerosp. Electron. Syst.* **2026**, doi: 10.1109/TAES.2026.3670773. (Early Access)
36. Gao F.; Li Y.; He X.; Sun J.; Wang J.; Hussain A. O2Former : direction-aware and multi-scale query enhancement for SAR ship instance segmentation. *IEEE J. Sel. Top. Appl. Earth Obs. Remote Sens*. **2026**, doi: 10.1109/JSTARS.2026.3677088. (Early Access)